Correlation function metrology for warm dense matter: Recent developments and practical guidelines

M. P. Böhme, ^{1, a)} W. M. Martin, ^{2, 3} H. M. Bellenbaum, ^{4, 5, 6} M. Berrens, ¹ J. Vorberger, ⁵ S. Schwalbe, ^{4, 5} Zh. A. Moldabekov, ^{4, 5} Th. Gawne, ^{4, 5} S. Hamel, ¹ B. Aguilar-Solis, ⁷ A. Sharma, ⁸ F. R. Graziani, ⁹ T. Döppner, ⁹ S. H. Glenzer, ³ T. Dornheim, ^{4, 5} and D. T. Bishel ^{9, b)}

X-ray Thomson scattering (XRTS) has emerged as a valuable diagnostic for matter under extreme conditions, as it captures the intricate many-body physics of the probed sample. Recent advances, such as the model-free temperature diagnostic of *Dornheim et al.* [Nat. Commun. 13, 7911 (2022)], have demonstrated how much information can be extracted directly within the imaginary-time formalism. However, since the imaginary-time formalism is a concept often difficult to grasp, we provide here a systematic overview of its theoretical foundations and explicitly demonstrate its practical applications to temperature inference, including relevant subtleties. Furthermore, we present recent developments that enable the determination of the absolute normalization, Rayleigh weight, and density from XRTS measurements without reliance on uncontrolled model assumptions. Finally, we outline a unified workflow that guides the extraction of these key observables, offering a practical framework for applying the method to interpret experimental measurements.

I. INTRODUCTION

Diagnostics of dense plasmas are of paramount importance to understand the microscopic states of matter at extreme conditions where Coulomb coupling, partial ionization, and quantum degeneracy all play decisive roles^{1–3}. In this non-ideal warm dense matter (WDM) regime, many standard approximations break down, so robust constraints from experiment are essential. X-ray Thomson scattering (XRTS) has become a premier probe for this purpose, enabling access to collective and single-particle excitations and, e.g., through detailed-balance, to thermodynamic information^{4–7}.

The central observable in XRTS is the electronic dynamic structure factor (DSF), which represents the correlations of density fluctuations within the system. Current experimental platforms have enabled the measurement of XRTS spectra using both backlighter X-ray sources^{8–11} and X-ray free electron lasers (XFELs) within the last two decades^{12–16}. Experimental spectra are typically interpreted via forward modeling, in which a model combining theoretical predictions and experimental effects is fitted to the measured data¹⁷. One of the most com-

monly used theories to model the DSF is the Chihara decomposition^{7,18,19}. The primary ansatz of the Chihara decomposition is the separation of the electronic density operator into bound and free contributions to compute a DSF for a given charge state, density and temperature^{20–23}. This ansatz requires precise knowledge of the microscopic electronic states in the plasma²⁴. Chihara models are often based on approximations within ground state theories or within the ideal plasma regime that have not been sufficiently tested for application to WDM. The approximations can therefore be inaccurate at thermal energies of several eVs and high compression rates, where excited states and non-ideal effects can be expected.

One prominent example is the effect of ionization potential depression (IPD), which refers to the lowering of the effective binding energy of bound states in a plasma environment. Several experimental studies have shown that effective ionization energies under WDM conditions are not predicted accurately^{5,25–29} by commonly used models such as the Ecker-Köll³⁰ or Stewart-Pyatt models³¹. The models treat screening from surrounding particles only as a uniform background and do not encompass the many-body quantum effects that are prominent in WDM. To expand our understanding of the behavior of bound electrons under extreme conditions, first principles studies have been conducted using advanced techniques such as average atom models³² (AA) and den-

¹⁾ Quantum Simulations Group, Physics and Life Science Directorate, Lawrence Livermore National Laboratory (LLNL), California 94550 Livermore, USA

²⁾Physics Department, Stanford University, Stanford, California 94305, USA

³⁾ SLAC National Accelerator Laboratory, Menlo Park California 94309, USA

⁴⁾ Center for Advanced Systems Understanding (CASUS), D-02826 Görlitz, Germany

⁵⁾ Helmholtz-Zentrum Dresden-Rossendorf (HZDR), D-01328 Dresden, Germany

⁶⁾Institut für Physik, Universität Rostock, D-18057 Rostock, Germany

⁷⁾ University of California, Merced, 5200 North Lake Road, Merced, CA 95343, USA

⁸⁾ Department of Civil Engineering, Indian Institute of Technology Roorkee, Roorkee, India

⁹⁾NIF and Photon Science, Lawrence Livermore National Laboratory (LLNL), 94550 Livermore California, USA

a) Electronic mail: boehme4@llnl.gov

b) Electronic mail: bishel1@llnl.gov

sity functional theory calculations^{33–35}. However, these studies also include several approximations and model assumptions that require rigorous testing in non-ideal regimes such as WDM. While recent path-integral Monte Carlo (PIMC) studies for the case of hydrogen^{2,23,36} have extracted ionization energies from quasi-exact simulations, the accessible system sizes remain limited to tens of ions due to PIMC's exponential computational costs³⁷. This example demonstrates the difficulties in the modeling of experiments in the WDM regime.

Recently, a complementary route formulated in the imaginary-time domain has proven especially power ful^{38-40} . By recasting the problem in terms of the imaginary-time correlation function (ITCF), which is the Laplace transform of the dynamic structure factor, one can exploit the numerical stability of Laplace space and directly leverage equilibrium symmetry ^{38,39,41}. This has led to a model-free temperature diagnostic and reliable uncertainty quantification even for noisy data 11,15,41-43. Beyond temperature, the imaginary-time framework provides a natural path to the a priori unknown absolute normalization of the measured XRTS spectrum via the universal f-sum rule⁴⁴. This, in turn, gives one access to the electronic static structure factor $S_{ee}(k)$, opening the door to additional observables such as the Rayleigh weight and static density response, all of which can be directly related to the measured spectra 41,45,46. The ITCF framework has already been used to refine physical modeling (e.g., identifying free-bound signatures relevant for equation-of-state measurements¹⁹) and to detect out-ofequilibrium states⁴⁷. At the same time, progress on forward modeling and instrument characterization continues to improve the fidelity of the combined source-andinstrument function (SIF) and thus the robustness of any remaining deconvolution step^{13,48}. Together, these developments delineate a correlation-function-centric metrology for WDM that is both mathematically rigorous and broadly applicable across experimental platforms.

Although this method is both powerful and straightforward to implement, its origin in first-principles quantum Monte Carlo studies $^{39,49-52}$, may make it less accessible to a broad audience. To encourage wider adoption, we take a pedagogical approach: we review the method's origins and provide a worked example that extracts temperature from an experimental spectrum using the imaginary-time formalism. We also introduce absolute normalization via the f-sum rule, enabling inference of the electronic static structure factor $S_{ee}(\mathbf{k})$ and, in turn, the Rayleigh weight $W_R(\mathbf{k})$. In addition, we present a diagnostic for non-equilibrium conditions in XRTS measurements. Overall, this work offers a methodological synopsis of imaginary-time techniques in the WDM context.

We first provide an overview of the methods used in this work and their connection to the experimental measurements. Figure (1) summarizes the workflow developed in Refs. $^{15,38,41,43-47}$. We start from the measured intensity $I(\mathbf{k},\omega)$ together with a model or measurement

of the SIF $R(\omega)$; the theoretical foundations of the measurement process are reviewed in Sec. II A. Next, we obtain the deconvolved, unnormalized ITCF from $I(\mathbf{k}, \omega)$ and $R(\omega)$. The methodology is introduced in Sec. II C and illustrated on an example measurement in Sec. III A based on Ref. 14. Even without normalization, the ITCF $F_{u}(\mathbf{k},\tau)$ enables temperature estimation and diagnosis of non-equilibrium when scattering is measured at multiple angles, as discussed in Sec. III E. To exploit the full diagnostic power of the ITCF, proper normalization is essential. We reiterate the theoretical basis in Sec. IIIB from Ref. 44 and show how it enables computation of the static structure factor $S_{ee}(\mathbf{k})$. This, in turn, allows extraction of the Rayleigh weight $W_R(\mathbf{k})$, presented in Sec. III C. W_R provides insight into electron localization and enables inference of the sample density from first principles⁴³. A complementary approach based on the imaginary-time fluctuation-dissipation theorem, described in Sec. IIID, requires only the area under the normalized ITCF $L(\mathbf{k})^{45}$. Overall, the workflow demonstrates how to obtain the key observables T, $S_{ee}(\mathbf{k})$, and $W_R(\mathbf{k})$ from first principles without uncontrolled model assumptions, provided the SIF $R(\omega)$ is accurately known. To infer the density ρ , the workflow requires a comparison against theoretical calculations and outlines two independent ways of inferring the density^{43,45}. This enables a consistency check of the theories and increases the robustness of the approach.

In summary, Sec. II gives the reader a brief overview of the origin of imaginary-time methods and their relation to measurements in real frequency space. The main part of this work is presented in Sec. III, where we provide a detailed example of how to compute the ITCF, along with a discussion of the associated subtleties and potential pitfalls. We conclude in Sec. IV with an outlook on leveraging these developments for multidiagnostic and multi-angle extensions¹⁵. We aim to promote a better understanding of the ITCF method as a reliable means of characterizing the full plasma state.

II. THEORY

In this section, we give an overview of the DSF, which governs the physics of XRTS. We review the physical measurement process to show the difference between the DSF and the recorded spectrum. In the last part of this section, we focus on the intricate connection between the DSF and the imaginary-time formalism. All the following derivations are done in Hartree atomic units ($\hbar=m_e=e=4\pi\varepsilon_0=1$).

A. X-ray Thomson scattering

XRTS experimental setups consist of an X-ray source, commonly a laser-driven foil or an XFEL beam, that probes a sample with the wavevector \mathbf{k}_i and a detec-

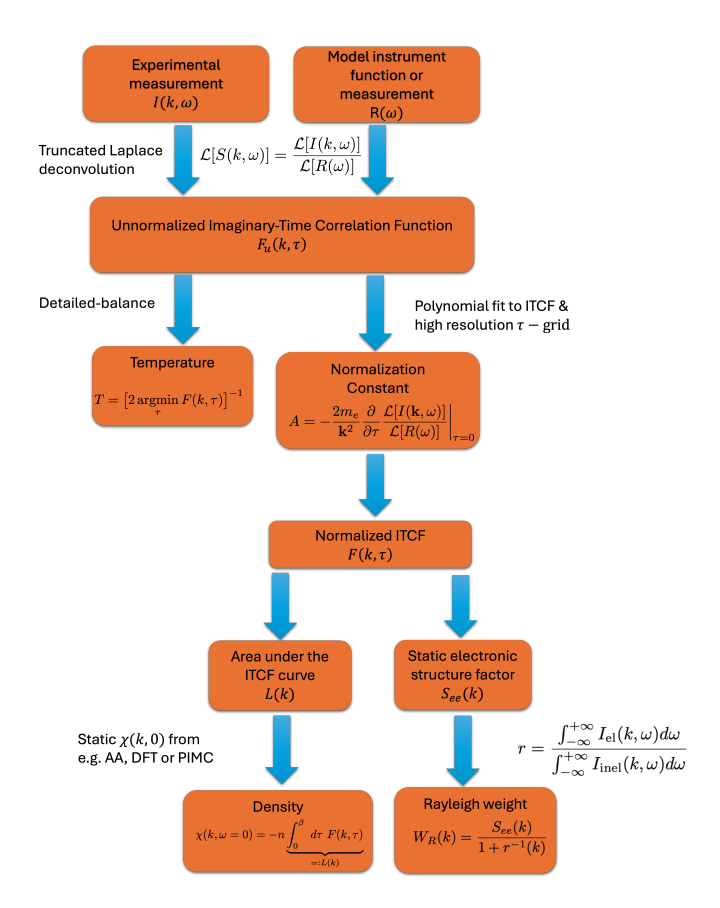


FIG. 1. Workflow for correlation-function metrology from XRTS. Starting from the measured intensity $I(\mathbf{k},\omega)$ and a measured or modeled source—and—instrument function (SIF) $R(\omega)$, a truncated two-sided Laplace deconvolution yields the (unnormalized) imaginary-time correlation function (ITCF) $F_n(\mathbf{k},\tau)$. Detailed-balance symmetry fixes the temperature via the location of the minimum at $\tau = \beta/2$. The $\tau \to 0$ slope, through the f-sum rule, provides the absolute normalization. The normalized ITCF supplies $S_{ee}(\mathbf{k}) = F(\mathbf{k}, 0)$ and, via Eq. (37), access to the static density response. Combining $S_{ee}(k)$ with the elastic/inelastic ratio gives the Rayleigh weight $W_R(\mathbf{k})$, while comparison of $\chi(\mathbf{k},0)$ to theoretical benchmarks enables density inference. Convergence with respect to the deconvolution window and the τ -grid, together with accurate SIF characterization, are the only analysis prerequisites.

tor that records the final wave-vector \mathbf{k}_s . The scattering wave vector is given by $\mathbf{k} = \mathbf{k}_s - \mathbf{k}_i$. The process of a photon getting scattered with a wave vector \mathbf{k} and a frequency ω is described by the differential cross-section¹⁸

$$\frac{\partial^2 \sigma}{\partial \Omega \partial \omega}(\mathbf{k}, \omega) = \sigma_T \frac{k_s}{k_i} S_{ee}(\mathbf{k}, \omega), \tag{1}$$

with $\sigma_T = 6.65 \times 10^{-29} \text{ m}^2$ the total Thomson cross-section and $S_{ee}(\mathbf{k},\omega)$ the electronic dynamical structure factor of the system. Interactions in WDM are commonly non-relativistic and quasi-elastic. As a result, the variables remain constant, and the physics is contained within the DSF. These assumptions break down for optical Thom-

son scattering and X-ray energies of 10 keV and more. The DSF is a quantity that represents the equilibrium density fluctuations of the system. To be precise, it is the Fourier transform of the intermediate scattering function for a system consisting of two particle species a and b:

$$S_{ab}(\mathbf{k},\omega) = \frac{1}{2\pi} \int_{-\infty}^{+\infty} dt \ F_{ab}(\mathbf{k},t) e^{i\omega t}, \tag{2}$$

with the intermediate scattering function defined as

$$F_{ab}(\mathbf{k},t) = \frac{1}{\sqrt{N_a N_b}} \langle \hat{\rho}_a(\mathbf{k},t) \hat{\rho}_b^*(\mathbf{k},0) \rangle.$$
 (3)

One should note that the average in Eq. (3) is to be understood as the thermal average within the canonical ensemble as

$$\langle A \rangle = \text{Tr} \left[\frac{e^{-\beta \hat{H}}}{Z} \hat{A} \right],$$
 (4)

where Z is the canonical partition function, \hat{H} represents the many-body Hamiltonian of the system, $\beta = (k_B T)^{-1}$ the inverse thermal energy and Tr[...] is the trace operator. We review the canonical partition function more in-depth in the next subsection. $\rho_a(\mathbf{k},t)$ are the particle density operator in the Heisenberg picture for particles a

$$\hat{\rho}_a(\mathbf{k},t) = e^{i\hat{H}t} \left[\sum_{i=1}^{N_a} e^{i\mathbf{k}\mathbf{r}_i} \right] e^{-i\hat{H}t}, \tag{5}$$

which is often referred to as the density fluctuations of the system. In the case of the electronic dynamic structure factor, the density operators are commonly split up into contributions from bound and free electrons

$$\rho(\mathbf{k}) = \rho_{\text{bound}}(\mathbf{k}) + \rho_{\text{free}}(\mathbf{k}), \tag{6}$$

which culminates in the Chihara decomposition¹⁸ when applying this ansatz to Eq. (3). One should note that the splitting of the electrons into bound and free populations is often difficult and not unique in the case of dense plasmas as orbital overlaps can make this decomposition ambiguous. This is caused by the resulting delocalization of bound electronic states, which makes these almost indistinguishable from continuum states.

One important insight is gained through an alternative definition of the DSF, the so-called spectral decomposition 53,54

$$S(\mathbf{k},\omega) = \frac{1}{Z} \sum_{n,m} e^{-\beta E_m} |\langle n | \hat{\rho}(\mathbf{k}) | m \rangle|^2 \delta(\omega - \omega_{mn}) , \quad (7)$$

where n,m refers to a sum over all the possible manybody eigenstates of the full Hamiltonian, E_m the eigenenergy of the m-th eigenstate of \hat{H} and ω_{nm} the energy difference between the states. By exchanging $n \neq m$, inserting $1 = e^{\beta\omega} e^{-\beta\omega}$, and using the evenness in Eq. (7) of the delta-function, we arrive at the detailed balance relation⁵³

$$S(\mathbf{k}, -\omega) = e^{-\beta \omega} S(\mathbf{k}, \omega) . \tag{8}$$

The above relation reveals a central symmetry in the theory of equilibrium density fluctuations that, in principle, we can utilize to obtain a temperature of any XRTS measurement⁶.

In practice, this is generally not directly applicable, as the measurement process must be performed using an X-ray beam of finite bandwidth and broadening from the instrument. As a result, the detector does not record the DSF itself, but rather its convolution with the SIF $R(\omega)^{13,55,56}$

$$I(\mathbf{k},\omega) = S(\mathbf{k},\omega) \otimes R(\omega) = \int_{-\infty}^{\infty} d\omega' S(\mathbf{k},\omega - \omega') R(\omega').$$
(9)

The SIF accounts for the spectral content of the source and broadening effects of the detection instrument, such as the mosaicity of a crystal analyzer⁵⁵. To truly infer temperature from Eq. (8) one must first deconvolve the DSF from the measured signal.

B. Origin of imaginary-time methods

Since the ITCF method³⁸ is inspired by the imaginarytime path-integral Monte Carlo (PIMC) method^{49,57,58}, we wish to give the reader a brief overview on the basic concepts that define imaginary time.

The real-time propagator of a system with a time-independent Hamiltonian \hat{H} is defined as

$$K(x_a, t_a; x_b, t_b) = \langle x_a | e^{-i\hat{H}(t_a - t_b)} | x_b \rangle, \tag{10}$$

for a system to transition from coordinate x_a at time t_a to x_b at t_b . If we now take the propagator that computes the conditional probability of a system transition $|x_a\rangle \rightarrow |x_b\rangle$ in between times 0 and t, we have

$$K(x_a, t; x_b, 0) = \langle x_a | e^{-i\hat{H}t} | x_b \rangle. \tag{11}$$

We can now perform a Wick rotation $t \rightarrow -i\tau$ with $\tau \in [0,\beta]$ of this expression and obtain the so-called imaginary-time propagator

$$K(x_a, \tau; x_b, 0) = \langle x_a | e^{-\tau \hat{H}} | x_b \rangle. \tag{12}$$

The canonical partition function

$$Z = \int dx \langle x | e^{-\tau \hat{H}} | x \rangle \Big|_{\tau = \beta} = \text{Tr} \left[e^{-\beta \hat{H}} \right], \quad (13)$$

is obtained by summing over all possible positions in the configuration space for distinguishable particles at temperature $\beta=(k_BT)^{-1}$ for a system transitioning back into its original state. Thus, for equilibrium systems, the real-time dynamics of closed paths connects to the statistical averages of the system. This fact is further discussed in Ref.⁵⁹.

It is well known from statistical mechanics that one can obtain any ensemble average from the partition function.

In principle, Eq. (13) enables us to calculate all equilibrium ensemble averages of the system from a trace over the density operator Eq. (4). This includes the density-density corelation function of the system. However, a particularly useful feature of the imaginary-time formalism reveals itself if one expands the partition function into P imaginary-time slices, which allows an accurate evaluation even for complex many-body systems. For simplicity, we focus here on the case of distinguishable particles. The observations remain the same in the case of indistinguishable particles. Let $\mathbf{R} = (\mathbf{r}_1, \mathbf{r}_2, \dots, \mathbf{r}_N)^T$ be the shorthand notation to include all spatial integration coordinates of the N-particles. The corresponding partition function can be expanded by inserting P-1 spatial unities into an alternative form

$$Z = \int d\mathbf{R} d\mathbf{R}_{1} \dots d\mathbf{R}_{P-1} \langle \mathbf{R} | e^{-\varepsilon \hat{H}} | \mathbf{R}_{1} \rangle$$

$$\times \langle \mathbf{R}_{1} | e^{-\varepsilon \hat{H}} | \mathbf{R}_{2} \rangle \dots \langle \mathbf{R}_{P-1} | e^{-\varepsilon \hat{H}} | \mathbf{R} \rangle$$

$$= \int d\mathbf{R} d\mathbf{R}_{1} \dots d\mathbf{R}_{P-1} \prod_{i=0}^{P-1} \rho(\mathbf{R}_{i}, \mathbf{R}_{i+1}; \varepsilon), \quad (14)$$

where $\varepsilon = \beta/P = (Pk_BT)^{-1}$ and P denotes the number of the discretizations steps of the imaginary-time axis. This expansion is essentially a Wick rotation of the Feynman path-integral⁶⁰. Since the Wick rotation preserves all information about the equilibrium system, we must be able to obtain all possible information from it³⁹. Eq. (14) describes the paths of multiple particles in imaginary-time that are connected by the high-temperature densitymatrix elements $\rho(\mathbf{R}_i, \mathbf{R}_{i+1}; \varepsilon)$. A conceptual picture of this is shown in Fig. 2.

This is the starting point of how to derive highly efficient sampling schemes for the partition function such as path-integral Monte Carlo $(PIMC)^{62,63}$.

C. Imaginary-time correlation functions

An important avenue opened by Eq. (14) is the possibility to calculate the equilibrium density fluctuations of the system from the thermal average defined by Eq. (4)

$$F(\mathbf{k},\tau) = \langle \hat{n}(\mathbf{k},0)\hat{n}(-\mathbf{k},\tau)\rangle, \tag{15}$$

which describes the density diffusion of particles within imaginary time where $\hat{n}(\mathbf{k},\tau)$ refers to the imaginary-time density particle operator. This function is called the imaginary-time correlation function (ITCF). It is defined analogously to Eq. (5). Since we only performed a Wick rotation of the real-time propagator, Eq. (15) must contain the same physical information as the real-time density-density intermediate scattering function Eq. (3). In an experiment, the density fluctuations of the system can be probed by scattering experiments under the assumption that the probe beam is sufficiently weak to not significantly influence the sample equilibrium distribution. A scattering experiment will measure not the

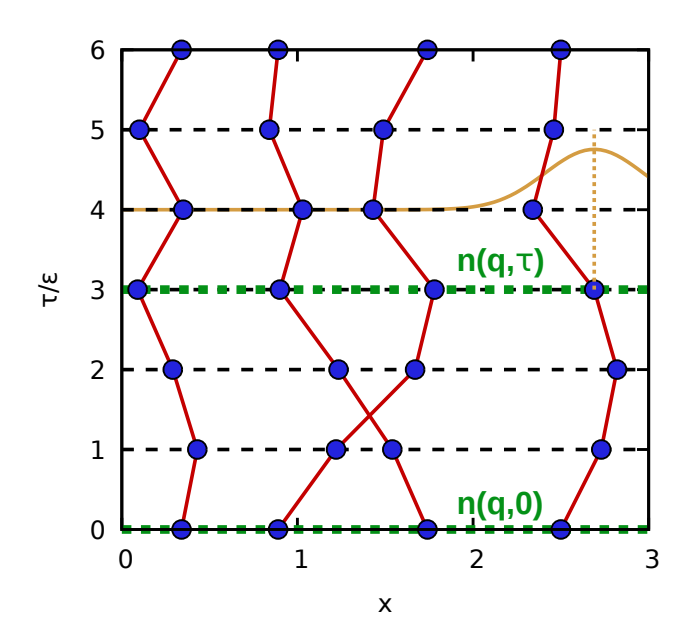


FIG. 2. Schematic picture of the imaginary-time evolution of 4 particles in one dimension. The spatial dimension is depicted here as the x-axis while the imaginary time axis τ is shown here in units of expansion steps ε . Each particle path is closed with respect to $x(0) = x(\beta) = x(6\epsilon)$. Note that the second and third particles are involved in a so-called permutation cycle⁶¹ and form a single intertwined path with the same 2β -periodic boundary conditions. Figure taken from Ref.³⁹ with the permission of the authors.

real-time intermediate scattering function Eq. (3), but the dynamic structure factor Eq. (2). The connection between the DSF and the ITCF is given by performing the inverse Fourier transformation in Eq. (2) and a Wick rotation that results in a two-sided Laplace transform

$$F(\mathbf{k},\tau) = \int_{-\infty}^{+\infty} d\omega \ S(\mathbf{k},\omega) e^{-\tau\omega} = \mathcal{L}[S(\mathbf{k},\omega)]. \tag{16}$$

The full calculation to arrive at this result requires some technical steps and results from complex analysis that we do not reiterate for simplicity. This equation tells us that in order to compare the results from an ensemble averaged simulation with the real-time measurements, we have to perform an inverse Laplace transformation ⁶⁴.

Inversion of such class of transformations are unfortunately a notoriously difficult, exponentially ill-posed problem that, so far, has been solved rigorously only in special cases⁶⁵. Recent promising advances have shown remarkable results such as a second roton feature of the uniform electron gas^{66–68}, but a general solution to the analytic continuation problem currently remains out of reach. Elevated from its original context, Eq. (16) has been reinterpreted in Ref.³⁸ to circumvent this problem entirely. As both the imaginary-time and real-frequency representation of any correlator must contain the same physical information, it is important to note that one can simply compute the ITCF from any measurement of

 $S(\mathbf{k},\omega)$. Thus, the ITCF as well as the DSF is sensitive to the system parameters and may be used to infer system parameters or otherwise gain insight into the system. As we discussed in the previous subsection, experiments do not probe the DSF directly, but rather the convolution between the SIF and the DSF. Therefore, in order to access the temperature information contained in the spectrum one has to also obtain a deconvolved ITCF. In contrast to Fourier space, deconvolution in the Laplace domain is more stable with respect to the experimental noise. One can use the analogous identity to the Fourier deconvolution in Laplace space

$$\mathcal{L}[S(\mathbf{k},\omega)](\tau) = \frac{\mathcal{L}[S(\mathbf{k},\omega) \otimes R(\omega)]}{\mathcal{L}[R(\omega)]}, \quad (17)$$

where the functional operator $\mathcal{L}[\cdot]$ refers to the two sided Laplace transformation, defined by

$$\mathcal{L}[h(\omega)](\tau) = \int_{-\infty}^{+\infty} d\omega \ h(\omega) \ e^{-\tau\omega}. \tag{18}$$

Eq. (17) reveals that in order to infer the full information in XRTS, one must have precise knowledge of the SIF $R(\omega)$. This problem persists also in forward modeling, where the convolution of a theoretical DSF model and $R(\omega)$ is fit to the measured intensity signal. Unfortunately, in certain experimental setups, e.g., at the NIF, one does not have direct access to $R(\omega)$ during the experiment and it has to be modeled 55,56 or characterized in a different campaign⁸. In the following section we will go through a practical example on how to utilize the ITCF for inferring the temperature.

To enhance the readers general understanding of the ITCF as a correlation function object, we show a schematic example of the typical curve shape of an ITCF in Fig. 3. The blue curve depicts the general shape of an ITCF, which is symmetric around $\beta/2$ in thermal equilibrium by detailed balance [Eq. (8)]. This can be shown by applying Eq. (8) to Eq. (16):

$$F(\mathbf{k},\tau) = \int_{-\infty}^{\infty} d\omega \ e^{-\tau\omega} \ S(\mathbf{k},\omega)$$

$$= \int_{0}^{\infty} d\omega \left(e^{-\tau\omega} S(\mathbf{k},\omega) + S(\mathbf{k},-\omega) e^{\tau\omega} \right)$$

$$= \int_{0}^{\infty} d\omega \ S(\mathbf{k},\omega) \left(e^{-\tau\omega} + e^{-\omega(\beta-\tau)} \right)$$

$$= F(\mathbf{k},\beta-\tau). \tag{19}$$

Therefore, if one can compute the exact ITCF from a measurement, the temperature immediately follows from the symmetry point of the ITCF using

$$k_B T = \frac{1}{2\tau_{\min}},\tag{20}$$

where $\tau_{\rm min}$ refers to the location of the minimum of the ITCF.

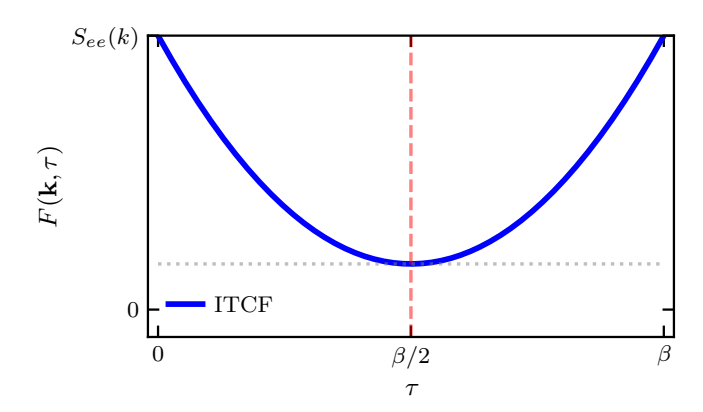


FIG. 3. Schematic curve shape of an ITCF shown in blue. The ITCF is a well defined correlation function on the imaginary-time axis $\tau \in [0, \beta]$. The minimum at $\beta/2$ is shown as the red dashed line. An important point of a properly normalized ITCF is at its origin value at $\tau=0$, which coincides with the total static structure factor of the system.

Additionally, the value of the ITCF at $\tau=0$ corresponds to the total static structure factor (SSF) $S(\mathbf{k})$ of the system:

$$F(\mathbf{k},0) = \int_{-\infty}^{+\infty} d\omega \ S(\mathbf{k},\omega) = S(\mathbf{k}). \tag{21}$$

This fact is leveraged in Sec. IIIB to infer the proper normalization of the ITCF from the (unnormalized) Laplace transform of the experimentally measured DSF.

We stress here again that the deconvolved ITCF from Eq. (17) does not immediately deliver the SSF but must be normalized to adhere to the f-sum rule. Therefore, the ITCF is a useful object that delivers insights into the equilibrium properties of system and can be computed immediately from experimental measurements for the case of a precisely known SIF.

III. METHODS

We start with the spectrum recorded in the experimental campaign reported by Martin et al. ⁶⁹ for diamond heated by a short-pulse laser. The spectrum is shown as the red curve in Fig. 4 and the SIF is depicted by the green curve normalized to the peak height of the measurement. We aligned the SIF peak at the reported measurement energy of 8160 eV⁶⁹. The reported inferred temperature for this particular data set was $T=61^{+27}_{-19}$ eV based on a Markov-Chain Monte Carlo analysis using a standard Chihara model assuming a charge state of Z=4. The spectrum was recorded at LCLS using a spectrometer placed at 170° resulting in a wave-vector of $k=8.24\,\text{Å}^{-1}$ and therefore in a non-collective scattering geometry.

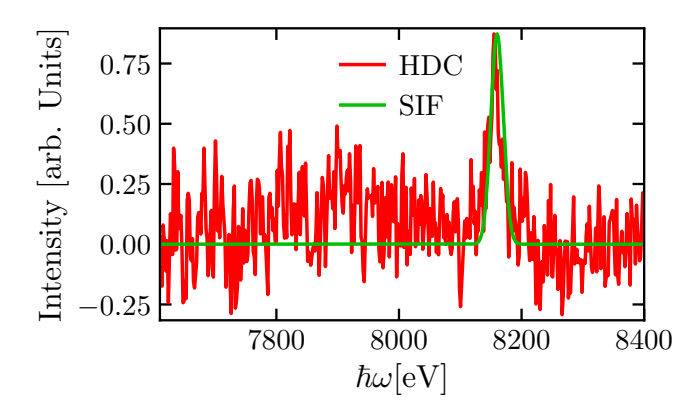


FIG. 4. XRTS spectrum in arbitrary units of heated diamond as reported in Ref. 69 . The green curve shows the corresponding source-and-instrument function (SIF) for the reported shot. The spectrum was recorded with a beam energy of 8160 eV at a scattering angle of 170° .

A. Temperature from the ITCF

The following considerations have to be made to obtain the Laplace deconvolved version of the spectrum. Experiments measure the density fluctuations of the plasma using a beam at a certain probe energy ω_i . The nature of scattering experiments dictates that the detected energies of the scattered photons ω_s are connected to the physical frequency axis by

$$\omega_s = \omega_i - \omega. \tag{22}$$

All theories describing the DSFs are defined with respect to ω , which represents the internal transition between states, while the scattering signal is recorded with respect to the scattered radiation frequency ω_s . In this work, we use the convention to refer to the downshifted part of the spectrum for $\omega > 0$ and the upshifted part of the spectrum as $\omega < 0$. This convention is motivated by the fact that an observed photon with frequency ω_s get red-shifted for the case of $\omega > 0$ and blue-shifted for $\omega < 0$ compared to the incoming photon of frequency ω_i . Therefore, one has to align the measurement spectrum to $\omega = 0$ by subtracting the probe beam energy and invert the energy axis, such that the down-shifted part of the spectrum and the upshifted part of the spectrum are aligned at $\omega > 0$ and $\omega < 0$, respectively. The same must be done for the SIF. Fig. 5 (a) depicts how the spectrum and SIF must be aligned. We then calculate the deconvolved ITCF and obtain a temperature. A vital practical detail for this calculation is that formally the deconvolution in Laplace space involves an infinite integral as shown in Eq. (17). However, detector setups in practice only allow to cover a finite amount of photon energies. Consequently, we have to truncate the Laplace deconvolution at a finite value x

$$\mathcal{L}_x[S(\mathbf{k},\omega)] = \frac{\mathcal{L}_x[S(\mathbf{k},\omega) \otimes R(\omega)]}{\mathcal{L}_{x'}[R(\omega)]},$$
 (23)

with the truncated two-sided Laplace transform defined

$$\mathcal{L}_x[S(\omega)](\tau) = \int_{-x}^{x} d\omega \ S(\omega) e^{-\omega \tau}. \tag{24}$$

It is important to note here that the Laplace transformation of $R(\omega)$ can be converged independent of the chosen truncation limit x of the experimental spectrum. We therefore denote the truncation of the $R(\omega)$ Laplacian with x'. For the deconvolution, we use a model SIF as in Ref.⁶⁹ of the form

$$R(\omega) = \sqrt{\frac{\ln 2}{\pi}} \frac{1}{\alpha} \exp\left[\frac{-(\omega - \omega_i)^2}{\alpha^2} \ln 2\right], \quad (25)$$

with $\omega_i = 8160 eV$ and $\alpha = 12$. The result of the deconvolution is shown in panel (c) of Fig. 5. The panel shows the ITCF of the data from the previous panel for a cutoff energy of x = 300 eV as a function of the imaginary time τ . The computed ITCF curve exhibits a clear symmetry around its minimum. This is a direct consequence of detailed balance in the DSF Eq. (8). Equation (19) shows that detailed-balance directly implies that the ITCF must be symmetric at $\tau = \beta/2$ of the system temperature and also has a minimum there. It therefore enables us to directly infer the presumed temperature of the system if we have a recorded XRTS intensity and a sufficient truncation interval. However, to obtain an accurate temperature, one cannot truncate the Laplace deconvolution arbitrarily, but must check which truncation is sufficient until the temperature remains roughly constant.

Panel (b) of Fig. 5 shows the inferred temperature from Eq. (23) as a function of the truncation parameter x. Because of the low SNR, the deconvolution reliably resolves detailed balance only for truncations in the range 229–377 eV. The inferred temperature begins to oscillate about a mean for x > 254 eV. We therefore estimate the temperature and its systematic uncertainty by taking the average and standard deviation of the inferred values for $254 \le x \le 377 \text{ eV}$, yielding $\bar{T} = 85 \pm 13 \text{ eV}$ (standard deviation). In Fig. Fig. 5(b), the red curve shows the temperature estimated at each truncation limit x; the blue dash-dotted line and shaded region depict \overline{T} and its systematic uncertainty. For comparison, our estimate is consistent with the analysis of Ref. 14 (green dotted line with shaded uncertainties), which reported $T = 61^{+27}_{-19}$ eV. A prominent feature in panel (b) is a sudden decrease in the inferred temperature for $x \in [376, 389]$ eV. In this interval the noise level prevents a reliable computation of the ITCF; the ITCF monotonically decreases, and no minimum is found. Consequently, temperatures inferred with truncation values in this range are unreliable. Beyond this interval the curve suggests some recovery of detailed balance, but the higher noise level in the data leads us to exclude those truncations from the average. Because the upshifted feature extends only up to an energy transfer of -403 eV, the detector range precludes larger truncations. Accordingly, while our result agrees

with Ref. ¹⁴, it should be regarded as an estimate. We determine that a higher SNR is required for a conclusive result. Nevertheless, the partial recovery of detailed balance and consistency with prior results indicate that the Laplace transform is relatively robust to noise. Consequently, the ITCF approach still yields meaningful estimates and provides a straightforward way to quantify uncertainty of temperatures from data with high noise or limited photon-counting statistics.

In summary, to infer temperature using detailed-balance from an XRTS spectrum, one must take the following practical steps

- 1. Align both the spectrum and the SIF to $\omega = 0$ by subtracting the probe energy.
- 2. Multiply the energy axis by -1 to correctly align the up- and downshifted feature with negative and positive frequencies, respectively.
- 3. Define a grid $\tau \in [0, \tau_{max}]$ of sufficient resolution.
- 4. Define a truncation range grid $x \in [0, x_{max}]$, and calculate for each grid point the ITCF on the τ grid from Eq. (23). Note down each $\tau_{min}(x) = \beta(x)/2 = [2k_BT(x)]^{-1}$.
- 5. Check if the temperature converges on the x grid and if the ITCF is symmetric for the converged points. If yes, the converged answer is the inferred temperature.
- 6. If the temperature converges up to a certain point on the x grid and then diverges, check if the ITCF is still symmetric around $\beta/2$ beyond these points. One may adjust the upper bound of the τ -grid and its resolution to see if the divergence still exists.
- 7. If the ITCF starts to become more asymmetric with an increasing integration boundary, one must check if the resolution of the upshifted feature is still sufficient or the experimental conditions are not in equilibrium.
- 8. If the inferred temperature exhibits oscillatory behavior within an interval as in Fig. 5 (c), detailed balance is only resolved in the measurement up to a certain cutoff. One then can average over the aforementioned interval and compute the standard deviation to estimate the temperature and its systematic uncertainty.

This exercise shows that the computation of temperature using the ITCF is not only simple, but also robust against noise. A corollary of this method is to reconstruct the temperature with a high degree of certainty, one must know the SIF of the measurement setup as precisely as possible as it is the only assumed quantity in the calculation. Furthermore, the symmetry in the ITCF directly reflects how well detailed-balance and therefore local thermal equilibrium is preserved in the measurement

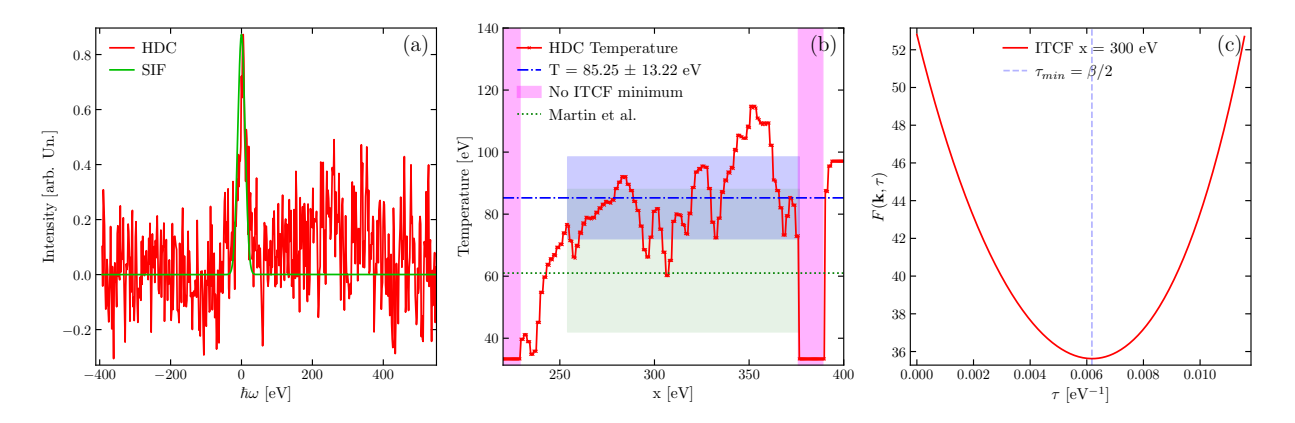


FIG. 5. Temperature analysis of the heated diamond spectrum reported in Ref. ⁶⁹. Panel (a) depicts the reported spectrum (red curve) and SIF (green curve) aligned to $\omega=0$ eV and with the energy axis multiplied by -1 to correctly align the downand upshifted energies on the positive and negative axis, respectively. Panel (b) shows the inferred temperature from the ITCF as a function of the truncation. Due to the low SNR of the signal, the deconvolution is only able to resolve detailed balance for truncations between 229 and 377 eV. The average inferred temperature within this range is given by $\bar{T}=85.25\pm13.22$ eV and shown as the blue dash-dotted line and the corresponding systematic uncertainties as the blue shaded band. The green dashed line depicts the inferred temperature in Ref. ⁶⁹ of $T=61^{+27}_{-19}$ eV, where the green shaded band depicts the uncertainties. The sudden drop in the inferred temperature between 376 and 389 eV is attributed to the high noise in this interval, which prevents the resolution of detailed balance. Panel (a) depicts the corresponding areas also by the magenta color. Panel (c) shows the calculated ITCF for a truncation of 300 eV and the vertical blue dashed line represents the location of the minimum.

data. The ITCF is not only useful to infer the temperature of the system, but can also be used to gain further physical insights.

However, one important note here is that the ITCF calculated with a cutoff, that does not cover the whole spectral range of the XRTS spectrum, is not the physical ITCF of the system. For instance, the ITCF shown in Fig. 5 (c) does not reflect the real ITCF of the system because the truncation of the deconvolution is not sufficiently large to cover the whole recorded spectrum. The extracted ITCF rather is a correlation function that obeys the same detailed balance relationship as the full ITCF, which still enables estimate of a temperature. Due to the low SNR in Fig. 5, the subsequent methods cannot be applied directly, and we therefore will proceed using a synthetic spectrum.

B. Obtaining the absolute normalization from the f-sum rule

We now compute the absolute normalization of the inferred ITCF, following the approach of Ref. 44 . The goal of this exercise is to obtain an absolute normalization from the f-sum rule without requiring a fully deconvolved DSF. Issues arise due to Eq. (17) only determining the ITCF up to a normalization factor A defined as

$$AF(\mathbf{k},\tau) = F_{\text{exp.}}(\mathbf{k},\tau) = \frac{\mathcal{L}[S(\mathbf{k},\omega) \otimes R(\omega)]}{\mathcal{L}[R(\omega)]}.$$
 (26)

 $F_{\rm exp.}$ refers to the experimentally inferred ITCF, which differs in normalization from the ITCF of Eq. (15) by only the normalization constant A.

We define the frequency moment of degree α of the DSF by

$$M_{\alpha}^{S} = \int_{-\infty}^{+\infty} S(\mathbf{k}, \omega) \omega^{\alpha} d\omega.$$
 (27)

The f-sum ${\rm rule}^{53}$ states that the first frequency moment of the DSF given by

$$M_1^S = \int_{-\infty}^{+\infty} d\omega \ S(\mathbf{k}, \omega) \omega$$
$$= -\frac{\partial}{\partial \tau} \frac{\mathcal{L}[S(\mathbf{k}, \omega) \otimes R(\omega)]}{\mathcal{L}[R(\omega)]} \bigg|_{\tau=0} = \frac{\mathbf{k}^2}{2m_e}, \tag{28}$$

must be obeyed due to particle number conservation. Since the f-sum rule has to be obeyed for all \mathbf{k} , we can define an absolute normalization of the ITCF that ensures the f-sum rule holds from a measurement at a single scattering angle. This is done by connecting the first frequency moment of the DSF to the ITCF given by

$$A = -\frac{2m_e}{\mathbf{k}^2} \frac{\partial}{\partial \tau} \frac{\mathcal{L}[I(\mathbf{k}, \omega)]}{\mathcal{L}[R(\omega)]} \bigg|_{\mathbf{k}^2} . \tag{29}$$

In practice, this requires that the spectra have been measured over an energy range such that the limits of the Laplace integral are effectively infinite, and with sufficient signal to distinguish the data from the background.

To demonstrate how to obtain the absolute normalization for a spectrum, we computed a spectrum using the Chihara decomposition^{7,18} for $C^{4.5+}$ at T=86 eV, $\rho=5$ gcm⁻³ and $\Theta=170^{\circ}$ in the top panel of Fig. 6. The bottom panel depicts the corresponding deconvolved ITCF where we chose a truncation of 1330 eV as any higher

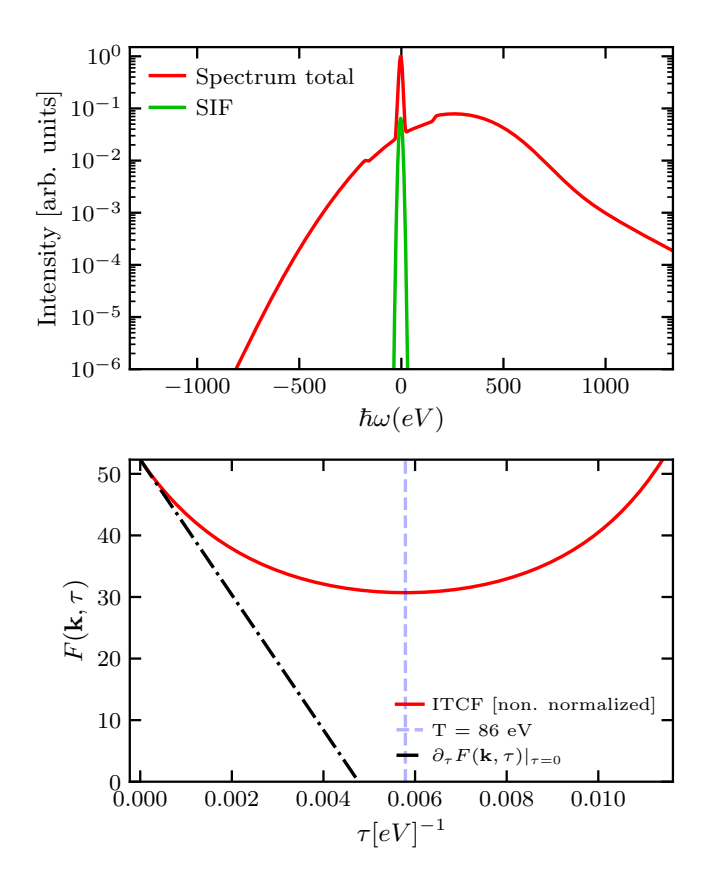


FIG. 6. Synthetic XRTS spectrum of $C^{4.5+}$ at T=86 eV, $\rho=5$ g cm⁻³, $\Theta=170^{\circ}$ calculated using the Chihara decomposition⁷. The lower panel depicts the corresponding ITCF integrated within the interval $\omega \in [-1330, 1330]$ eV. The black dashed-dotted line depicts the slope of the ITCF derivative at $\tau=0$ needed to obtain the normalization constant from the f-sum rule.

cutoff will result in issues with resolution of the downshifted feature due to numerical instabilities of floating point operations. The cutoff sufficiently resolves both the upshifted and downshifted feature to calculate an accurate ITCF, shown in the lower panel. The black dashed-dotted line depicts the slope of the τ = 0 derivative using a forward numerical derivative, that we require for the normalization constant. In Hartree atomic units, we require the square of the scattering wave-vector that we can approximate if the incoming and outgoing frequencies $\omega_i/\omega_s \approx 1^{41}$

$$k \equiv |\mathbf{k}| \approx 2k_0 \sin(\Theta/2). \tag{30}$$

In our case, we have $k_0 = \omega/c = E_0/\hbar c = 4.14 \times 10^{10} \text{ m}^{-1}$. Thus the wave-number is given by $k = 8.24 \times 10^{10} \text{ m}^{-1} = 4.36 a_B^{-1}$.

The normalization of the ITCF opens a pathway to many practical applications^{45,46}, such as the extraction of the density response function and inference of the mass density. Refs.^{43,45} also introduce another practical way to obtain both the normalization and the electron-electron static structure factor (SSF) $S_{ee}(k)$. Comparing the def-

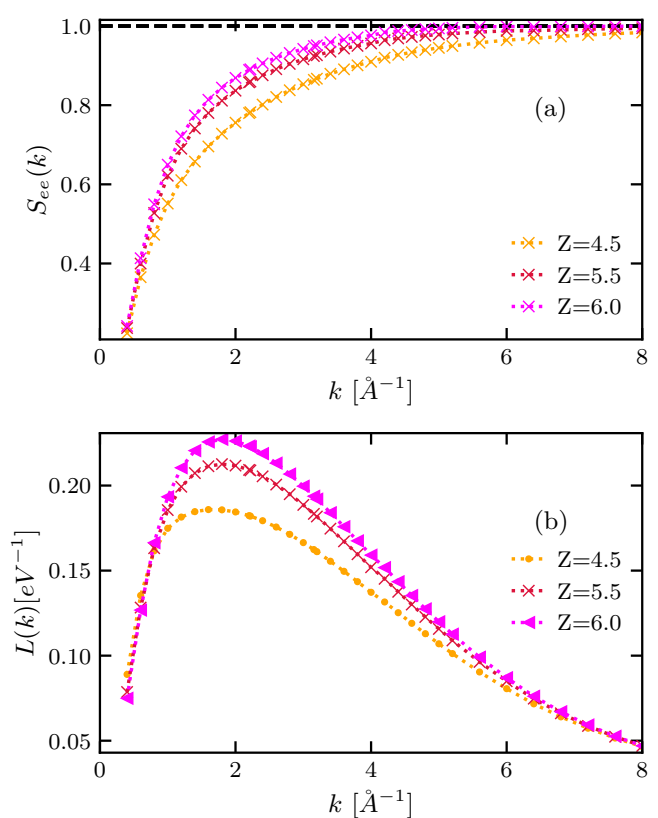


FIG. 7. Panel (a) depicts the static structure factor of carbon as a function of the wave-vector for several charge states at $\rho = 5 \text{ g cm}^{-3}$ and T = 86 eV computed from the Chihara decomposition. Panel (b) depicts the resulting area under the ITCF curve from the same conditions.

inition of $S_{ee}(k)$ with $F(k,\tau)$

$$S_{ee}(k) = \int_{-\infty}^{+\infty} d\omega \ S_{ee}(k,\omega)$$
$$= M_0^S(k) = F(k,0), \tag{31}$$

implies that the absolute normalization of the ITCF immediately delivers the static electronic structure factor.

We show the SSF for this example in C at several ionization degrees in Fig. 7 panel (a). $S_{ee}(k)$ shows the expected behavior of converging towards unity for large wavenumbers k. From a practical perspective, calculating the SSF and the normalization from Eqs. (29) and (31) involves an integration close to $\tau = 0$. Consequently, computing the SSF and the normalization is more robust with respect to the SNR of the upshifted part of the spectrum. One of the central results in Ref. 44 is that the slope in the ITCF can be too steep to allow for practical calculations using a simple forward numerical derivative. A more practical and accurate approach is to use a polynomial fit in order to compute the $\tau = 0$ derivative⁷⁰. The convergence behavior of the static structure factor for carbon is shown as an example for the case of $C^{4.5+}$ at $k = 8\mathring{A}$ in Fig. 9.

C. Obtaining the Rayleigh weight

We present how to practically extract the Rayleigh weight W_R from measurements^{43,46}. W_R itself is a measure of the total electronic localisation around the nuclei in a plasma. For instance, in the Chiahara decomposition, it reflects the amount of elastic scattering from electrons localised around the ions

$$S^{\text{Ch.}}(k,\omega) = S_{\text{inel.}}(k,\omega) + W_R^{\text{Ch.}}(k)\delta(\omega).$$
 (32)

Furthermore $W_R(\mathbf{k})$ is generally defined as⁷¹

$$W_R(k) = \frac{S_{eI}^2(k)}{S_{II}(k)},\tag{33}$$

where $S_{eI}(k)$ refers to the electron-ion static structure factor and $S_{II}(k)$ refers to the ion-ion static structure factor. In the aforementioned Chihara decomposition the Rayleigh weight is modeled as²⁰

$$W_R^{\text{Ch.}}(k) = \sum_{a,b} \sqrt{n_a n_b} |f_a(k) + q_a(k)| |f_b(k) + q_b(k)| S_{ab}(k),$$
(34)

with the a,b sum over all ion species in the plasma, $n_{a,b}$ being the partial density of the plasma, $f_{a,b}(k)$ the ionic form factor, $q_{a,b}(k)$ the corresponding screening cloud and $S_{ab}(k)$ the corresponding ion-ion static structure factor.

A common observable that can be extracted from precise knowledge of the SIF is the ratio of elastic to inelastic scattering, obtained by decomposing the spectrum into its elastic and inelastic components. For this exercise, one only has to obtain a fit of the experimental spectrum that accurately can capture the elastic feature and compute

$$r = \frac{\int_{-\infty}^{+\infty} I_{\text{el}}(k,\omega) d\omega}{\int_{-\infty}^{+\infty} I_{\text{inel}}(k,\omega) d\omega} = \frac{W_R(k)}{S_{ee}(k) - W_R(k)}.$$
 (35)

Due to the knowledge of $S_{ee}(k)$ from Eqs. (29) and (31), we can infer the Rayleigh weight by

$$W_R(k) = \frac{S_{ee}(k)}{1 + r^{-1}(k)},\tag{36}$$

from known quantities that can be computed cheaply without any model assumptions. This approach has opened up a way to successfully infer densities from XRTS experiments at the National Ignition Facility (NIF) for beryllium capsule implosions 9,43 . Additionally, the knowledge of W_R opens avenues to discriminate between model assumptions that are often used in WDM calculations, such as different exchange-correlation functionals. An example is depicted in Fig. 8. The figure shows the Rayleigh weight computed from density functional theory using the SPARC code 72,73 with spectral partitioning 74 at 150 eV for various wave-numbers at different densities. This is compared to the experimental

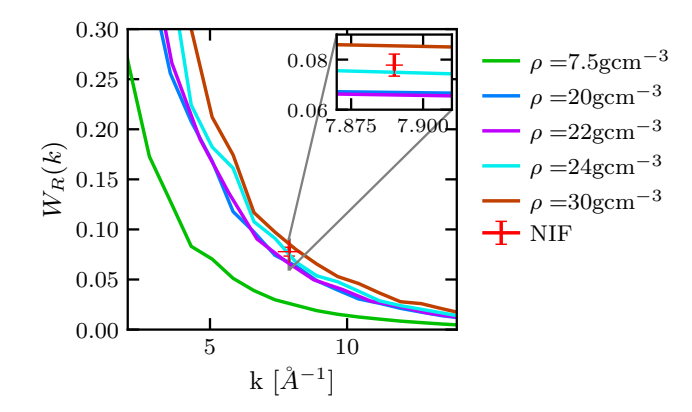


FIG. 8. Rayleigh weight of warm dense beryllium as a function of scattering wave-vector. The red cross shows the data point reported for the NIF shot in Ref.⁹. The curves show a corresponding calculation of the Rayleigh weight from spectral partitioning DFT⁷⁴ using the PBE functional⁷⁵ at 7.5, 20, 22, 24 and 30 g/cm^3 for a temperature of 150 eV.

data point obtained in Ref.⁹, which is shown as the red cross. The curve suggest that the density of the sample must be between 20 gcm⁻³ and 30 gcm⁻³. This is in good agreement with the results found in Ref.⁴⁶.

D. Area under the ITCF

A useful relation is the imaginary-time version of the fluctuation-dissipation theorem 39,45

$$\chi(k,\omega=0) = -n \underbrace{\int_0^\beta d\tau \ F(k,\tau)}_{=:L(k)}, \tag{37}$$

where $\chi(k,\omega)$ refers to the linear density response function 53,76. This equation reveals an interesting connection. The area under the ITCF curve L(k) is an experimental observable that can be computed as soon as the normalization Eq. (29) is obtained. The static density response function $\chi(k,0)$ on the left hand side Eq. (37) is an accessible quantity that can be calculated even from single-particle theories^{77–79}. Fig. 7 panel (b) depicts the behavior for the area under the ITCF for carbon computed using the Chihara decomposition. As shown in Schwalbe et al.⁴⁵, this calculation can then be utilized in comparison with different theories capable of calculating $\chi(k,0)$ to infer densities from experimental measurements. One important prerequisite for this comparison is that the ITCF is very well converged with respect to the truncation of Eq. (17). Panel (b) of Fig. 9 depicts the convergence of L(k) at $k = 8\mathring{A}^{-1}$ with respect to the truncation from synthetic Chihara spectra of $C^{4.5+}$. One can here use an exponential fit

$$f(x) = a + be^{cx}, (38)$$

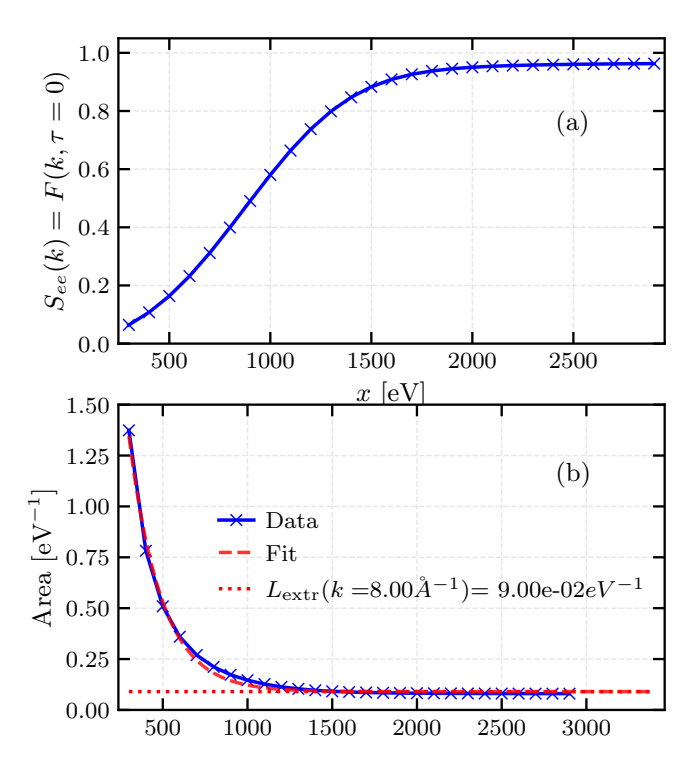


FIG. 9. Convergence behavior of the (a) static structure factor and (b) the area under the ITCF curve Eq. (39) for $C^{4.5+}$ for the conditions specified in Fig. 7 as a function of the truncation x as the blue crosses at $k=8\mathring{A}$. The red dashed line shows an exponential extrapolation fit to overcome the numerical limitation with the cutoff radius of the area under the ITCF curve. The vertical red dotted lines in each panel depict the asymptotic extrapolation for $x\to\infty$.

to overcome numerical or practical limitations, which is depicted as the red dashed curve. The extrapolated area under the ITCF curve is shown as the dotted red lines in the figure. As a practical method, Ref. ⁴⁵ introduces a two-fold convergence approach on how to practically obtain both the normalization and the SSF by introducing a double truncated Laplace deconvolution

$$\mathcal{L}_{x,y}[S(k,\omega)] = \int_{x}^{y} d\omega \ S(k,\omega) \ e^{-\tau\omega}. \tag{39}$$

This can now be used in the deconvolution integral

$$\mathcal{L}[S(k,\omega)] = \frac{\mathcal{L}_{x,y}[S(k,\omega) \otimes R(\omega)]}{\mathcal{L}_{x'}[R(\omega)]},$$
 (40)

where one must check the double-sided convergence of the deconvolution with respect to x and y. By employing this two-fold convergence, the ITCF can be captured with sufficient fidelity, and its normalization can be evaluated with the accuracy required to infer the density from Eq. (37).

In conjunction with Sec. III C, this enables two independent pathways for determining densities from XRTS spectra: one based on comparison with theoretical approaches capable of computing the Rayleigh weight, and

another relying on methods that provide the static density response function. Accordingly, the recommended practice for density inference from XRTS is to combine both approaches, drawing on distinct models or *ab initio* techniques. This integrated strategy establishes a robust framework for density determination that can be applied in a direct and systematic manner.

E. Detecting non-equilibrium for multiple scattering angles

As a last step, we are reviewing the most important results from Ref. ⁴⁷. So far all our computations relied on the fact that the DSF fulfills detailed balance as soon as the probed system is in local thermal equilibrium (LTE). The previous observation can be utilized to not only infer the equilibrium properties of a system, but also to detect non-equilibrium conditions once detailed balance is violated. One of the central results in Ref. ⁴⁷ is that the violation of the detailed-balance symmetry condition might not be possible to detect if the resolution of the experiment is insufficient, which may be the case for current experimental setups ¹⁵.

Therefore, the work suggests an advantageous pathway to detect non-equilibrium shown in Fig. 10. The first panel depicts the Wigner function of the electron gas for an equilibrium (green curve) and non-equilibrium situation (black curve). For this demonstration, we use the same model for the Wigner function with a hot electronic tail as in Ref. 47 given by

$$f(k,t) = A_c \left\{ \exp\left[\beta_c \left(\frac{k^2}{2m} - \mu_c\right)\right] \right\}^{-1} + A_h \left\{ \exp\left[\beta_h \left(\frac{k^2}{2m} - \mu_h\right)\right] \right\}^{-1}, \tag{41}$$

with component amplitude $A_{c,h}$ referring to the cold and hot spectra, $\beta_{c,h}$ the temperatures of the bulk and the hot electronic tail, with their individual chemical potential. Panel (a) displays the Wigner function Eq. (41) under equilibrium (green) and nonequilibrium (black) conditions. Panel (b) of Fig. 10 presents the corresponding dynamic structure factors (DSFs) for these Wigner functions. For wave-vectors $k = 0.2, 1.0 a_B^{-1}$, the equilibrium DSFs appear as green curves, while the nonequilibrium DSFs are represented by blue curves (collective regime) and red curves (non-collective regime). While the DSFs show very similar features, this changes in panel (c). Here both green curves show the same minimum in the equilibrium case and therefore adhere to detailed balance at the same temperature. However, this situation is completely different for the red curve, which depicts the non-eq. ITCF at $k=0.2a_B^{-1}$. While the curve itself seems to be largely symmetric around its minimum, the given minimum is notably not at the temperature of the electronic bulk. The the amount of violation with

respect to detailed-balance is not sufficient to detect non-equilibrium with certainty in this case. In contrast, the blue curve, that is plotted on a separate y-axis, clearly is not symmetric around its minimum and the location of the minimum disagrees with the red curve. Therefore, it is vital to observe that a symmetric ITCF at a single wavenumber is only a necessary condition for equilibrium. Instead, to establish a necessary and sufficient test of equilibrium, the ITCF at different scattering wavenumbers must all be symmetric about the same minimum in τ .

This remarkable result enables one to explore the non-equilibrium properties of WDM experimentally from first principles. Current experimental setups such as at the European XFEL could in principle be used to explore things such as equilibration times of pump-probe experiments. Other pump-probe experimental setups could be utilized under the condition that spectra are measured simultaneously from multiple scattering angles. A practical application of detecting equilibrium with two scattering angles on isochorically heated graphite has already been tried in Ref. however, the detector ranges of the presented experiments may have been insufficient. New experiments with modern detectors could deliver a sufficient detector range to resolve non-equilibrium states.

IV. SUMMARY AND DISCUSSION

We have presented a practical, largely model-free workflow to extract equilibrium and near-equilibrium plasma properties from X-ray Thomson scattering (XRTS) by working in imaginary time. The central step is to replace the ill-posed Fourier deconvolution in real frequency by a numerically stable two-sided Laplace deconvolution to obtain the imaginary-time correlation function (ITCF) $F(k,\tau)$. Within $F(k,\tau)$, detailed balance appears as a symmetry with a minimum at $\tau = \beta/2$, which enables direct and robust temperature inference^{38,41}. The $\tau \to 0$ slope fixes the absolute normalization via the f-sum rule $\overline{^{44}}$, and F(k,0) provides the static electronic structure factor $S_{ee}(k)$; integrating the ITCF yields Eq. (37), which gives access to the static density response⁴⁵. Together with an elastic/inelastic intensity ratio, these quantities yield the Rayleigh weight $W_R(k)$, and comparison of $\chi(k,0)$ to single-particle or first-principles benchmarks enables density inference and model validation^{43,45,46}. In short, the imaginary-time route turns XRTS into a correlation-function metrology that emphasizes stability and interpretability. We show a basic workflow on how all these observables can be extracted in a systematic flowchart in Fig. 1.

In practice, three ingredients are decisive for accurate results: (i) a well-characterized SIF, (ii) convergence checks with respect to the finite deconvolution window (preferably double-sided) and the τ -grid resolution, and (iii) adequate signal-to-noise in the downshifted feature to resolve detailed balance. Recent work

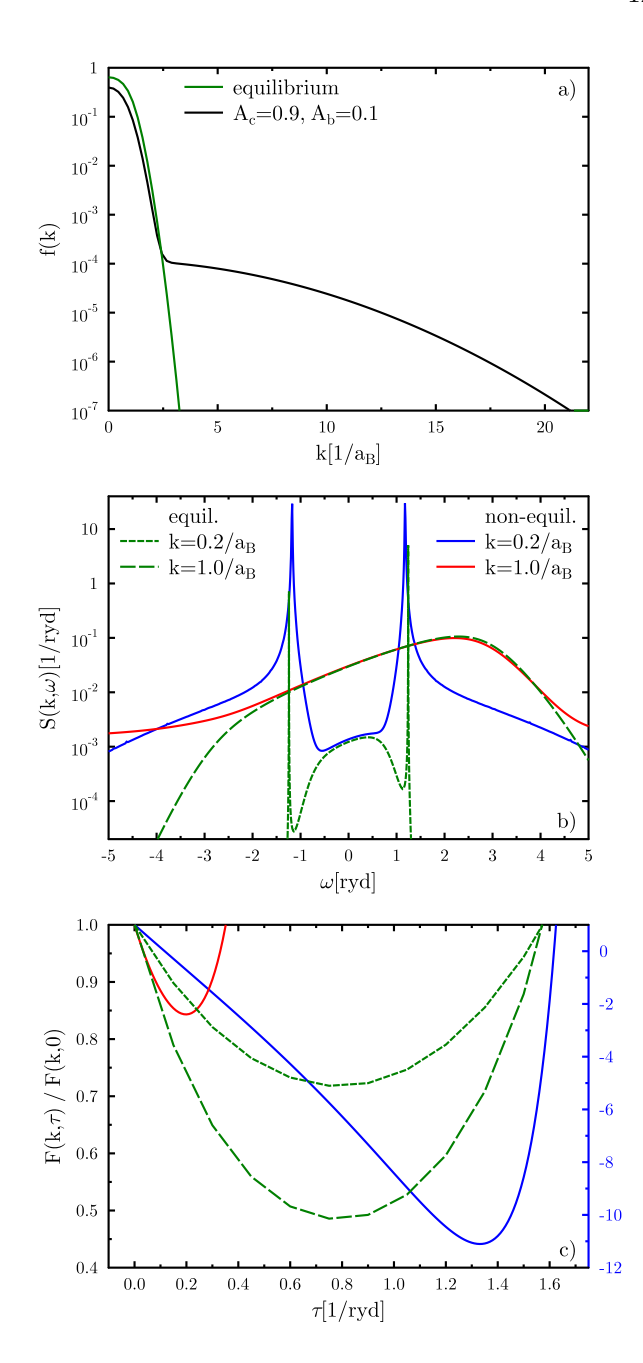


FIG. 10. Detection of non-equilibrium as suggested in Ref. 47. Panel (a) shows the Wigner function of the uniform electron gas for the equilibrium case denoted as the green curve and the non-equilibrium case as the black curve. The electronic density is as given in Ref. 47 by $n=1.8\times 10^{23}~{\rm cm}^{-3}$. The cold electronic bulk of the black curve was assigned a temperature of $T_c = 10^5$ K. The hot electron bump is located at $p_B = 25/a_B$ and models the non-equilibrium scenraio of the black curve with a temperature of $T_b = 10^4$ K. Panel (b) then denotes the corresponding DSF for two different scattering wave numbers in the collective and single particle regime. The equilibrium DSFs are given by both green curves, while the nonequilibrium DSFs are shown by the blue curve for the collective scattering regime and the red curve for the singleparticle regime. The subsequent panel (c) then shows the corresponding ITCFs of the four given curves. The blue curve is plotted on a separate scaled y-axis on the right hand side.

on mosaic-crystal spectrometers and ultrahigh-resolution XRTS underscores how SIF metrology and modeling sharpen ITCF-based diagnostics^{13,48,56}. When these criteria are met, the ITCF pipeline is remarkably tolerant to experimental noise and yields temperatures and normalizations consistent with independent analyses^{38,41,44}.

Beyond equilibrium diagnostics, the imaginary-time framework enables a straightforward test for non-equilibrium: violations of detailed balance manifest as shifts in the ITCF minima that vary with scattering vector k. A multi-angle strategy therefore provides a robust, first-principles indicator of relaxation dynamics in pump-probe and isochoric-heating experiments 15,47 . This ability to detect departures from local thermal equilibrium (and their restoration) is a distinctive strength of the ITCF approach.

Looking ahead, two approaches appear especially promising. First, standardizing SIF metrology and uncertainty quantification, together with automated convergence criteria for the truncated Laplace deconvolution will make ITCF-based analysis reliable across common ICF and XFEL platforms ^{13,48,56}, while routine multiangle collection will enable equilibrium checks and nonequilibrium studies in a single shot ¹⁵. Second, advances in analytic continuation (e.g., dual-form maximum entropy and kernel-representation methods) point toward reconstructing the full dynamic structure factor from high-quality ITCFs ^{67,80}, combined with *ab initio* benchmarks ^{65,77,78}, opening a path to validate approximate DSFs.

In short, we gain stability, interpretability, and extensibility by shifting XRTS analysis to imaginary time. Temperature, normalization, static structure, and non-equilibrium indicators become immediately accessible so that we ultimately can uncover the complex many-body physics of WDM.

ACKNOWLEDGMENTS

The work of M.P.B, D.T.B. and T.D. was performed under the auspices of the U.S. Department of Energy by Lawrence Livermore National Laboratory under Contract No. DE-AC52-07NA27344. M.P.B., D.T.B. and Ti.D. were supported by Laboratory Directed Research and Development (LDRD) Grant Nos. 24-ERD-044 and 25-ERD-047. This work was partially supported by the Center for Advanced Systems Understanding (CA-SUS), financed by Germany's Federal Ministry of Education and Research (BMBF) and the Saxon state government out of the State budget approved by the Saxon State Parliament. This work has received funding from the European Research Council (ERC) under the European Union's Horizon 2022 research and innovation programme (Grant agreement No. 101076233, "PREX-TREME"). Views and opinions expressed are however those of the authors only and do not necessarily reflect those of the European Union or the European Research Council Executive Agency. Neither the European Union nor the granting authority can be held responsible for them. This work has received funding from the European Union's Just Transition Fund (JTF) within the project Röntgenlaser-Optimierung der Laserfusion (ROLF), contract number 5086999001, co-financed by the Saxon state government out of the State budget approved by the Saxon State Parliament. W.M.M. acknowledges support from the National Science Foundation Graduate Research Fellowship Program under Grant No. DGE-2146755. This work was funded by the DOE Office of Science, Fusion Energy Science under FWP100182. We acknowledge support from Department of Energy (DOE), Office of Science, Fusion Energy Sciences, under Award No. DE-SC 0024882: IFE-STAR was issued as SLAC FWP 101126. The work of B.A.S. was supported by Department of Energy Award No. DE-SC0024476.

REFERENCES

¹J. Vorberger, F. Graziani, D. Riley, A. D. Baczewski, I. Baraffe, M. Bethkenhagen, S. Blouin, M. P. Böhme, M. Bonitz, M. Bussmann, A. Casner, W. Cayzac, P. Celliers, G. Chabrier, N. Chamel, D. Chapman, M. Chen, J. Clérouin, G. Collins, F. Coppari, T. Döppner, T. Dornheim, L. B. Fletcher, D. O. Gericke, S. Glenzer, A. F. Goncharov, G. Gregori, S. Hamel, S. B. Hansen, N. J. Hartley, S. Hu, O. A. Hurricane, V. V. Karasiev, J. J. Kas, B. Kettle, T. Kluge, M. D. Knudson, A. Kononov, Z. K. á, D. Kraus, A. Kritcher, S. Malko, G. Massacrier, B. Militzer, Z. A. Moldabekov, M. S. Murillo, B. Nagler, N. Nettelmann, P. Neumayer, B. K. Ofori-Okai, I. I. Oleynik, M. Preising, A. Pribram-Jones, T. Ramazanov, A. Ravasio, R. Redmer, B. Rethfeld, A. P. L. Robinson, G. Röpke, F. Soubiran, C. E. Starrett, G. Steinle-Neumann, P. A. Sterne, S. Tanaka, A. P. Thompson, S. B. Trickey, T. Vinci, S. M. Vinko, L. Wang, A. J. White, T. G. White, U. Zastrau, E. Zurek, P. Tolias, "Roadmap for warm dense matter physics," arXiv:2505.02494 [physics.plasm-ph].

²M. Bonitz, J. Vorberger, M. Bethkenhagen, M. P. Böhme, D. M. Ceperley, A. Filinov, T. Gawne, F. Graziani, G. Gregori, P. Hamann, S. B. Hansen, M. Holzmann, S. X. Hu, H. Kählert, V. V. Karasiev, U. Kleinschmidt, L. Kordts, C. Makait, B. Militzer, Z. A. Moldabekov, C. Pierleoni, M. Preising, K. Ramakrishna, R. Redmer, S. Schwalbe, P. Svensson, and T. Dornheim, "Toward first principles-based simulations of dense hydrogen," Physics of Plasmas 31, 110501 (2024), https://pubs.aip.org/aip/pop/article-pdf/doi/10.1063/5.0219405/20250831/110501_1_5.0219405.pdf.

³R. Drake, *High-Energy-Density Physics: Foundation of Inertial Fusion and Experimental Astrophysics*, Graduate Texts in Physics (Springer International Publishing, 2018).

⁴S. H. Glenzer and R. Redmer, "X-ray thomson scattering in high energy density plasmas," Rev. Mod. Phys 81, 1625 (2009).

⁵D. Kraus, B. Bachmann, B. Barbrel, R. W. Falcone, L. B. Fletcher, S. Frydrych, E. J. Gamboa, M. Gauthier, D. O. Gericke, S. H. Glenzer, S. Göde, E. Granados, N. J. Hartley, J. Helfrich, H. J. Lee, B. Nagler, A. Ravasio, W. Schumaker, J. Vorberger, and T. Döppner, "Characterizing the ionization potential depression in dense carbon plasmas with high-precision spectrally resolved x-ray scattering," Plasma Physics and Controlled Fusion 61, 014015 (2019).

⁶T. Döppner, O. Landen, H. Lee, P. Neumayer, S. Regan, and S. Glenzer, "Temperature measurement through detailed balance

in x-ray thomson scattering," High Energy Density Physics 5, 182-186 (2009).

⁷G. Gregori, S. H. Glenzer, W. Rozmus, R. W. Lee, and O. L. Landen, "Theoretical model of x-ray scattering as a dense matter probe," Phys. Rev. E 67, 026412 (2003).

⁸M. J. MacDonald, A. M. Saunders, B. Bachmann, M. Bethkenhagen, L. Divol, M. D. Doyle, L. B. Fletcher, S. H. Glenzer, D. Kraus, O. L. Landen, H. J. LeFevre, S. R. Klein, P. Neumayer, R. Redmer, M. Schörner, N. Whiting, R. W. Falcone, and T. Döppner, "Demonstration of a laser-driven, narrow spectral bandwidth x-ray source for collective x-ray scattering experiments," Physics of Plasmas 28, 032708 (2021).

 $^9\mathrm{T.}$ Döppner, M. Bethkenhagen, D. Kraus, P. Neumayer, D. A. Chapman, B. Bachmann, R. A. Baggott, M. P. Böhme, L. Divol, R. W. Falcone, L. B. Fletcher, O. L. Landen, M. J. MacDonald, A. M. Saunders, M. Schörner, P. A. Sterne, J. Vorberger, B. B. L. Witte, A. Yi, R. Redmer, S. H. Glenzer, and D. O. Gericke, "Observing the onset of pressure-driven k-shell delocalization," Nature (2023), 10.1038/s41586-023-05996-8.

¹⁰S. H. Glenzer, O. L. Landen, P. Neumayer, R. W. Lee, K. Widmann, S. W. Pollaine, R. J. Wallace, G. Gregori, A. Höll, T. Bornath, R. Thiele, V. Schwarz, W.-D. Kraeft, and R. Redmer, "Observations of plasmons in warm dense matter," Phys. Rev. Lett. 98, 065002 (2007).

 $^{11}\mathrm{N.}$ Y. Shi, J. H. Liang, C. J. Mo, D. Wu, X. H. Yuan, $\,$ and J. Zhang, "First-principles analysis of the warm dense plasma jets in double-cone ignition experiments," (2025), arXiv:2504.04317 [physics.plasm-ph].

¹²L. B. Fletcher, A. Kritcher, A. Pak, T. Ma, T. Döppner, C. Fortmann, L. Divol, O. L. Landen, J. Vorberger, D. A. Chapman, D. O. Gericke, R. W. Falcone, and S. H. Glenzer, "X-ray thomson scattering measurements of temperature and density from multi-shocked ch capsules," Physics of Plasmas 20, 056316 (2013), https://doi.org/10.1063/1.4807032.

¹³T. Gawne, Z. A. Moldabekov, O. S. Humphries, K. Appel, Baehtz, V. Bouffetier, E. Brambrink, A. Cangi, S. Göde, Z. Konôpková, M. Makita, M. Mishchenko, M. Nakatsutsumi, K. Ramakrishna, L. Randolph, S. Schwalbe, J. Vorberger, L. Wollenweber, U. Zastrau, T. Dornheim, and T. R. Preston, "Ultrahigh resolution x-ray thomson scattering measurements at the european x-ray free electron laser," Phys. Rev. B 109, L241112 (2024).

¹⁴W. M. Martin, J. Nilsen, L. B. Fletcher, M. J. MacDonald, L. Andersen, A. Arnott, H. Bellenbaum, M. Böhme, N. Boiadjieva, N. Czapla, T. E. Cowan, T. Döppner, G. Dyer, R. N. Ettelbrick, R. Falcone, S. Faubel, E. Galtier, A. Laso Garcia, T. Gawne, L. Hancock, P. Hart, N. J. Hartley, M. L. Herbert, X. Huang, G. Jain, K. D. Kabelitz, D. Khaghani, D. Kraus, H. J. Lee, P. Li, Y. Lu, M. Mettry-Yassa, P. McGehee, B. Nagler, J. Rips, S. Schumacher, E. R. Toro, T. Toncian, X. Xia, A. Gleason, and S. H. Glenzer, "Characterizing laser-heated polymer foams with simultaneous x-ray fluorescence spectroscopy and thomson scattering at the matter in extreme conditions endstation at lcls," Physics of Plasmas **32**, 072701 (2025).

¹⁵H. M. Bellenbaum, B. Bachmann, D. Kraus, T. Gawne, M. P. Böhme, T. Döppner, L. B. Fletcher, M. J. MacDonald, Z. A. Moldabekov, T. R. Preston, J. Vorberger, and T. Dornheim, "Toward model-free temperature diagnostics of warm dense matter from multiple scattering angles," Applied Physics Letters 126, 044104 (2025), https://pubs.aip.org/aip/apl/article $pdf/doi/10.1063/5.0248230/20365613/044104_1_5.0248230.pdf.$

¹⁶D. S. Bespalov, U. Zastrau, Z. A. Moldabekov, T. Gawne, T. Dornheim, M. Meshhal, A. Amouretti, M. Andrzejewski, K. Appel, C. Baehtz, E. Brambrink, K. Buakor, C. Camarda, D. Chin, G. Collins, C. Crepisson, A. Descamps, J. Eggert, L. Fletcher, A. Forte, G. Gregori, M. Harmand, O. S. Humphries, H. Hoeppner, J. Kuhlke, W. Lynn, J. Luetgert, M. Masruri, E. M. McBride, R. S. McWilliams, A. A. S. Mora, J.-P. Naedler, P. Neumayer, C. Palmer, A. Pelka, L. Pennacchioni, D. Polsin, C. Prestwood, N. A. Pukhareva, C. Qu, D. Ranjan, R. Redmer, M. Roeper, C. Sahle, S. Schumacher, J.-P. Schwinkendorf, M. J. Sieber, M. Singleton, E. Smith, C. Sternemann, T. Stevens, M. Stevenson, C. Strohm, M. Tang, M. Toncian, T. Toncian, T. Tschentscher, S. Vinko, J. Wark, M. Wilke, D. Kraus, and T. R. Preston, "Experimental validation of electron correlation models in warm dense matter," (2025), arXiv:2509.10107 [physics.plasm-ph].

¹⁷M. F. Kasim, T. P. Galligan, J. Topp-Mugglestone, G. Gregori, and S. M. Vinko, "Inverse problem instabilities in largescale modeling of matter in extreme conditions," Physics of Plasmas 26, 112706 (2019), https://pubs.aip.org/aip/pop/articlepdf/doi/10.1063/1.5125979/12607940/112706_1_online.pdf.

 $^{18}\mathrm{J}.$ Chihara, "Difference in x-ray scattering between metallic and non-metallic liquids due to conduction electrons," Journal of Physics F: Metal Physics 17, 295–304 (1987).

¹⁹M. P. Böhme, L. B. Fletcher, T. Döppner, D. Kraus, A. D. Baczewski, T. R. Preston, M. J. MacDonald, F. R. Graziani, Z. A. Moldabekov, J. Vorberger, and T. Dornheim, "Evidence of free-bound transitions in warm dense matter and their impact on equation-of-state measurements," (2023), arXiv:2306.17653 [physics.plasm-ph].

²⁰K. Wünsch, J. Vorberger, G. Gregori, and D. O. Gericke, "X-ray scattering as a probe for warm dense mixtures and high-pressure miscibility," EPL 94, 25001 (2011).

²¹D. A. Chapman, D. Kraus, A. L. Kritcher, B. Bachmann, G. W. Collins, R. W. Falcone, J. A. Gaffney, D. O. Gericke, S. H. Glenzer, T. M. Guymer, J. A. Hawreliak, O. L. Landen, S. Le Pape, T. Ma, P. Neumayer, J. Nilsen, A. Pak, R. Redmer, D. C. Swift, J. Vorberger, and T. Döppner, "Simulating x-ray thomson scattering signals from high-density, millimetre-scale plasmas at the national ignition facility," Physics of Plasmas 21, 082709 (2014).

²²D. A. Chapman, J. Vorberger, L. B. Fletcher, R. A. Baggott, L. Divol, T. Döppner, R. W. Falcone, S. H. Glenzer, G. Gregori, T. M. Guymer, A. L. Kritcher, O. L. Landen, T. Ma, A. E. Pak, and D. O. Gericke, "Observation of finite-wavelength screening in high-energy-density matter," Nature Communications 6 (2015), 10.1038/ncomms7839.

²³H. M. Bellenbaum, M. P. Böhme, M. Bonitz, T. Döppner, L. B. Fletcher, T. Gawne, D. Kraus, Z. A. Moldabekov, S. Schwalbe, J. Vorberger, and T. Dornheim, "Estimating ionization states and continuum lowering from ab initio path integral monte carlo simulations for warm dense hydrogen," Phys. Rev. Res. 7,033016

 $^{24}\mathrm{B.}$ A. Mattern and G. T. Seidler, "Theoretical treatments of the bound-free contribution and experimental best practice in x-ray thomson scattering from warm dense matter," Physics of Plasmas 20, 022706 (2013), https://pubs.aip.org/aip/pop/articlepdf/doi/10.1063/1.4790659/16147847/022706_1_online.pdf.

²⁵O. Ciricosta, S. M. Vinko, H.-K. Chung, C. Jackson, R. W. Lee, T. R. Preston, D. S. Rackstraw, and J. S. Wark, "Detailed model for hot-dense aluminum plasmas generated by an x-ray free electron laser," Physics of Plasmas 23, 022707 (2016), https://pubs.aip.org/aip/pop/article $pdf/doi/10.1063/1.4942540/15796915/022707_1_online.pdf.$

²⁶D. J. Hoarty, P. Allan, S. F. James, C. R. D. Brown, L. M. R. Hobbs, M. P. Hill, J. W. O. Harris, J. Morton, M. G. Brookes, R. Shepherd, J. Dunn, H. Chen, E. Von Marley, P. Beiersdorfer, H. K. Chung, R. W. Lee, G. Brown, and J. Emig, "Observations of the effect of ionization-potential depression in hot dense plasma," Phys. Rev. Lett. 110, 265003 (2013).

²⁷B. Crowley, "Continuum lowering – a new perspective," High Energy Density Physics 13, 84 – 102 (2014).

²⁸L. B. Fletcher, A. L. Kritcher, A. Pak, T. Ma, T. Döppner, C. Fortmann, L. Divol, O. S. Jones, O. L. Landen, H. A. Scott, J. Vorberger, D. A. Chapman, D. O. Gericke, B. A. Mattern, G. T. Seidler, G. Gregori, R. W. Falcone, and S. H. Glenzer, "Observations of continuum depression in warm dense matter with x-ray thomson scattering," Phys. Rev. Lett. 112, 145004 (2014).

 $^{29}\mathrm{C}.$ A. Iglesias, "A plea for a reexamination of ionization potential

- depression measurements," High Energy Density Physics **12**, 5 11 (2014).
- ³⁰G. Ecker and W. Kröll, "Lowering of the Ionization Energy for a Plasma in Thermodynamic Equilibrium," Physics of Fluids 6, 62–69 (1963).
- ³¹J. C. Stewart and J. Kedar D. Pyatt, "Lowering of Ionization Potentials in Plasmas," Astrophysical Journal 144, 1203 (1966).
- ³²G. Massacrier, M. Böhme, J. Vorberger, F. Soubiran, and B. Militzer, "Reconciling ionization energies and band gaps of warm dense matter derived with ab initio simulations and average atom models," Phys. Rev. Res. 3, 023026 (2021).
- ³³S. X. Hu, "Continuum lowering and fermi-surface rising in strongly coupled and degenerate plasmas," Phys. Rev. Lett. 119, 065001 (2017).
- ³⁴M. Bethkenhagen, B. B. L. Witte, M. Schörner, G. Röpke, T. Döppner, D. Kraus, S. H. Glenzer, P. A. Sterne, and R. Redmer, "Carbon ionization at gigabar pressures: An ab initio perspective on astrophysical high-density plasmas," Phys. Rev. Research 2, 023260 (2020).
- ³⁵T. Gawne, T. Campbell, A. Forte, P. Hollebon, G. Perez-Callejo, O. S. Humphries, O. Karnbach, M. F. Kasim, T. R. Preston, H. J. Lee, A. Miscampbell, Q. Y. van den Berg, B. Nagler, S. Ren, R. B. Royle, J. S. Wark, and S. M. Vinko, "Investigating mechanisms of state localization in highly ionized dense plasmas," Phys. Rev. E 108, 035210 (2023).
- ³⁶M. Bonitz and L. Kordts, "Ionization potential depression and fermi barrier in warm dense matter: A first-principles approach," Contributions to Plasma Physics n/a, e70001, https://onlinelibrary.wiley.com/doi/pdf/10.1002/ctpp.70001.
- ³⁷T. Dornheim, "Fermion sign problem in path integral Monte Carlo simulations: Quantum dots, ultracold atoms, and warm dense matter," Phys. Rev. E **100**, 023307 (2019).
- ³⁸T. Dornheim, M. Böhme, D. Kraus, T. Döppner, T. R. Preston, Z. A. Moldabekov, and J. Vorberger, "Accurate temperature diagnostics for matter under extreme conditions," Nature Communications 13, 7911 (2022).
- ³⁹T. Dornheim, Z. A. Moldabekov, P. Tolias, M. Böhme, and J. Vorberger, "Physical insights from imaginary-time density-density correlation functions," Matter and Radiation at Extremes 8, 056601 (2023), https://pubs.aip.org/aip/mre/articlepdf/doi/10.1063/5.0149638/18081889/056601_1_5.0149638.pdf.
- ⁴⁰T. Dornheim, J. Vorberger, Z. A. Moldabekov, and M. Böhme, "Analysing the dynamic structure of warm dense matter in the imaginary-time domain: theoretical models and simulations," Philosophical Transactions of the Royal Society A: Mathematical, Physical and Engineering Sciences 381, 20220217 (2023).
- ⁴¹T. Dornheim, M. P. Böhme, D. A. Chapman, D. Kraus, T. R. Preston, Z. A. Moldabekov, N. Schlünzen, A. Cangi, T. Döppner, and J. Vorberger, "Imaginary-time correlation function thermometry: A new, high-accuracy and model-free temperature analysis technique for x-ray thomson scattering data," Physics of Plasmas 30, 042707 (2023), https://pubs.aip.org/aip/pop/article-pdf/doi/10.1063/5.0139560/16832024/042707_1_5.0139560.pdf.
- ⁴²M. Schörner, M. Bethkenhagen, T. Döppner, D. Kraus, L. B. Fletcher, S. H. Glenzer, and R. Redmer, "X-ray thomson scattering spectra from density functional theory molecular dynamics simulations based on a modified chihara formula," Phys. Rev. E 107, 065207 (2023).
- ⁴³T. Dornheim, T. Döppner, P. Tolias, M. P. Böhme, L. B. Fletcher, T. Gawne, F. R. Graziani, D. Kraus, M. J. MacDonald, Z. A. Moldabekov, S. Schwalbe, D. O. Gericke, and J. Vorberger, "Unraveling electronic correlations in warm dense quantum plasmas," Nature Communications 16, 5103 (2025).
- ⁴⁴T. Dornheim, T. Döppner, A. D. Baczewski, P. Tolias, M. P. Böhme, Z. A. Moldabekov, T. Gawne, D. Ranjan, D. A. Chapman, M. J. MacDonald, T. R. Preston, D. Kraus, and J. Vorberger, "X-ray thomson scattering absolute intensity from the f-sum rule in the imaginary-time domain," Scientific Reports 14, 14377 (2024).

- ⁴⁵S. Schwalbe, H. Bellenbaum, T. Döppner, M. Böhme, T. Gawne, D. Kraus, M. J. MacDonald, Z. Moldabekov, P. Tolias, J. Vorberger, and T. Dornheim, "Static linear density response from x-ray thomson scattering measurements: a case study of warm dense beryllium," (2025), arXiv:2504.13611 [physics.plasm-ph].
- ⁴⁶T. Dornheim, H. M. Bellenbaum, M. Bethkenhagen, S. B. Hansen, M. P. Böhme, T. Döppner, L. B. Fletcher, T. Gawne, D. O. Gericke, S. Hamel, D. Kraus, M. J. MacDonald, Z. A. Moldabekov, T. R. Preston, R. Redmer, M. Schörner, S. Schwalbe, P. Tolias, and J. Vorberger, "Model-free rayleigh weight from x-ray thomson scattering measurements," Physics of Plasmas 32, 052712 (2025).
- ⁴⁷J. Vorberger, T. R. Preston, N. Medvedev, M. P. Böhme, Z. A. Moldabekov, D. Kraus, and T. Dornheim, "Revealing non-equilibrium and relaxation in laser heated matter," Physics Letters A 499, 129362 (2024).
- ⁴⁸T. Gawne, H. Bellenbaum, L. B. Fletcher, K. Appel, C. Baehtz, V. Bouffetier, E. Brambrink, D. Brown, A. Cangi, A. Descamps, S. Goede, N. J. Hartley, M.-L. Herbert, P. Hesselbach, H. Höppner, O. S. Humphries, Z. Konôpková, A. Laso Garcia, B. Lindqvist, J. Lütgert, M. J. MacDonald, M. Makita, W. Martin, M. Mishchenko, Z. A. Moldabekov, M. Nakatsutsumi, J.-P. Naedler, P. Neumayer, A. Pelka, C. Qu, L. Randolph, J. Rips, T. Toncian, J. Vorberger, L. Wollenweber, U. Zastrau, D. Kraus, T. R. Preston, and T. Dornheim, "Effects of mosaic crystal instrument functions on x-ray thomson scattering diagnostics," Journal of Applied Physics 136, 105902 (2024), https://pubs.aip.org/aip/jap/article-pdf/doi/10.1063/5.0222072/20150309/105902_1_5.0222072.pdf.
- ⁴⁹D. M. Ceperley, "Path integrals in the theory of condensed helium," Rev. Mod. Phys 67, 279 (1995).
- ⁵⁰A. Filinov, "Correlation effects and collective excitations in bosonic bilayers: Role of quantum statistics, superfluidity, and the dimerization transition," Phys. Rev. A 94, 013603 (2016).
- ⁵¹M. Boninsegni and D. M. Ceperley, "Density fluctuations in liquid4he. path integrals and maximum entropy," Journal of Low Temperature Physics 104, 339–357 (1996).
- ⁵²T. Dornheim, Z. A. Moldabekov, and J. Vorberger, "Nonlinear density response from imaginary-time correlation functions: Ab initio path integral monte carlo simulations of the warm dense electron gas," The Journal of Chemical Physics 155, 054110 (2021).
- ⁵³G. Giuliani and G. Vignale, Quantum Theory of the Electron Liquid (Cambridge University Press, Cambridge, 2008).
- ⁵⁴K. Sturm, "Dynamic structure factor: An introduction," Zeitschrift für Naturforschung A 48, 233–242 (1993).
- ⁵⁵T. Gawne, H. Bellenbaum, L. B. Fletcher, K. Appel, C. Baehtz, V. Bouffetier, E. Brambrink, D. Brown, A. Cangi, A. Descamps, S. Goede, N. J. Hartley, M.-L. Herbert, P. Hesselbach, H. Höppner, O. S. Humphries, Z. Konôpková, A. Laso Garcia, B. Lindqvist, J. Lütgert, M. J. MacDonald, M. Makita, W. Martin, M. Mishchenko, Z. A. Moldabekov, M. Nakatsutsumi, J.-P. Naedler, P. Neumayer, A. Pelka, C. Qu, L. Randolph, J. Rips, T. Toncian, J. Vorberger, L. Wollenweber, U. Zastrau, D. Kraus, T. R. Preston, and T. Dornheim, "Effects of mosaic crystal instrument functions on x-ray thomson scattering diagnostics," Journal of Applied Physics 136, 105902 (2024), https://pubs.aip.org/aip/jap/article-pdf/doi/10.1063/5.0222072/20150309/105902_1.5.0222072.pdf.
- ⁵⁶T. Gawne, S. Schwalbe, T. Chuna, U. H. Acosta, T. R. Preston, and T. Dornheim, "Heart: A new x-ray tracing code for mosaic crystal spectrometers," (2025), arXiv:2503.16955 [physics.plasm-ph].
- ⁵⁷M. F. Herman, E. J. Bruskin, and B. J. Berne, "On path integral monte carlo simulations," The Journal of Chemical Physics **76**, 5150–5155 (1982), https://doi.org/10.1063/1.442815.
- ⁵⁸M. Takahashi and M. Imada, "Monte carlo calculation of quantum systems," Journal of the Physical Society of Japan **53**, 963–974 (1984).
- $^{59}\mathrm{G}.$ Stefanucci and R. van Leeuwen, "The contour idea," in

- Nonequilibrium Many-Body Theory of Quantum Systems: A Modern Introduction (Cambridge University Press, 2025) p. 93–122.
- ⁶⁰H. Kleinert, Path Integrals in Quantum Mechanics, Statistics, Polymer Physics, and Financial Markets, EBL-Schweitzer (World Scientific, 2009).
- ⁶¹T. Dornheim, S. Groth, A. V. Filinov, and M. Bonitz, "Path integral monte carlo simulation of degenerate electrons: Permutation-cycle properties," The Journal of Chemical Physics 151, 014108 (2019), https://doi.org/10.1063/1.5093171.
- ⁶²M. Boninsegni, N. V. Prokofev, and B. V. Svistunov, "Worm algorithm and diagrammatic Monte Carlo: A new approach to continuous-space path integral Monte Carlo simulations," Phys. Rev. E 74, 036701 (2006).
- ⁶³M. Boninsegni, N. V. Prokofev, and B. V. Svistunov, "Worm algorithm for continuous-space path integral Monte Carlo simulations," Phys. Rev. Lett 96, 070601 (2006).
- ⁶⁴M. Jarrell and J. Gubernatis, "Bayesian inference and the analytic continuation of imaginary-time quantum monte carlo data," Phys. Rep. **269**, 133–195 (1996).
- ⁶⁵T. Dornheim, S. Groth, J. Vorberger, and M. Bonitz, "Ab initio path integral monte carlo results for the dynamic structure factor of correlated electrons: From the electron liquid to warm dense matter," Phys. Rev. Lett. 121, 255001 (2018).
- ⁶⁶T. M. Chuna, J. Vorberger, P. Tolias, A. Benedix Robles, M. Hecht, P.-A. Hofmann, Z. A. Moldabekov, and T. Dornheim, "Second roton feature in the strongly coupled electron liquid," The Journal of Chemical Physics 163, 034117 (2025), https://pubs.aip.org/aip/jcp/article-pdf/doi/10.1063/5.0281085/20597331/034117_1_5.0281085.pdf.
- ⁶⁷T. Chuna, N. Barnfield, T. Dornheim, M. P. Friedlander, and T. Hoheisel, "Dual formulation of the maximum entropy method applied to analytic continuation of quantum monte carlo data," Journal of Physics A: Mathematical and Theoretical 58, 335203 (2025).
- ⁶⁸T. Chuna, N. Barnfield, J. Vorberger, M. P. Friedlander, T. Hoheisel, and T. Dornheim, "Estimates of the dynamic structure factor for the finite temperature electron liquid via analytic continuation of path integral monte carlo data," Phys. Rev. B 112, 125112 (2025).
- ⁶⁹W. M. Martin, J. Nilsen, L. B. Fletcher, M. J. MacDonald, L. Andersen, A. Arnott, H. Bellenbaum, M. Böhme, N. Boiadjieva, N. Czapla, T. E. Cowan, T. Döppner, G. Dyer, R. N. Ettelbrick, R. Falcone, S. Faubel, E. Galtier, A. Laso Garcia, T. Gawne, L. Hancock, P. Hart, N. J. Hartley, M. L. Herbert, X. Huang, G. Jain, K. D. Kabelitz, D. Khaghani, D. Kraus, H. J. Lee, P. Li, Y. Lu, M. Mettry-Yassa, P. McGehee, B. Nagler, J. Rips, S. Schumacher, E. R. Toro, T. Toncian, X. Xia, A. Gleason, and S. H. Glenzer, "Characteriz-

- ing laser-heated polymer foams with simultaneous x-ray fluorescence spectroscopy and thomson scattering at the matter in extreme conditions endstation at lcls," Physics of Plasmas **32**, 072701 (2025), https://pubs.aip.org/aip/pop/article-pdf/doi/10.1063/5.0267033/20575594/072701_1_5.0267033.pdf.
- ⁷⁰T. Dornheim, D. C. Wicaksono, J. E. Suarez-Cardona, P. Tolias, M. P. Böhme, Z. A. Moldabekov, M. Hecht, and J. Vorberger, "Extraction of the frequency moments of spectral densities from imaginary-time correlation function data," Phys. Rev. B 107, 155148 (2023).
- ⁷¹J. Vorberger and D. O. Gericke, "Ab initio approach to model x-ray diffraction in warm dense matter," Phys. Rev. E **91**, 033112 (2015).
- ⁷²Q. Xu, A. Sharma, B. Comer, H. Huang, E. Chow, A. J. Medford, J. E. Pask, and P. Suryanarayana, "Sparc: Simulation package for ab-initio real-space calculations," SoftwareX 15, 100709 (2021).
- ⁷³B. Zhang, X. Jing, Q. Xu, S. Kumar, A. Sharma, L. Erlandson, S. J. Sahoo, E. Chow, A. J. Medford, J. E. Pask, and P. Suryanarayana, "Sparc v2.0.0: Spin-orbit coupling, dispersion interactions, and advanced exchange—correlation functionals," Software Impacts 20, 100649 (2024).
- ⁷⁴B. Sadigh, D. Åberg, and J. Pask, "Spectral-partitioned kohn-sham density functional theory," Phys. Rev. E **108**, 045204 (2023).
- ⁷⁵J. P. Perdew, K. Burke, and M. Ernzerhof, "Generalized gradient approximation made simple," Phys. Rev. Lett. **77**, 3865–3868 (1996).
- ⁷⁶T. Dornheim, Z. A. Moldabekov, K. Ramakrishna, P. Tolias, A. D. Baczewski, D. Kraus, T. R. Preston, D. A. Chapman, M. P. Böhme, T. Döppner, F. Graziani, M. Bonitz, A. Cangi, and J. Vorberger, "Electronic density response of warm dense matter," Physics of Plasmas 30 (2023), 10.1063/5.0138955, 032705.
- ⁷⁷M. Böhme, Z. A. Moldabekov, J. Vorberger, and T. Dornheim, "Ab initio path integral monte carlo simulations of hydrogen snapshots at warm dense matter conditions," Phys. Rev. E 107, 015206 (2023).
- ⁷⁸M. Böhme, Z. A. Moldabekov, J. Vorberger, and T. Dornheim, "Static electronic density response of warm dense hydrogen: Ab initio path integral monte carlo simulations," Phys. Rev. Lett. 129, 066402 (2022).
- ⁷⁹Z. Moldabekov, M. Böhme, J. Vorberger, D. Blaschke, and T. Dornheim, "Ab initio static exchange—correlation kernel across jacob's ladder without functional derivatives," Journal of Chemical Theory and Computation 19, 1286–1299 (2023), pMID: 36724889, https://doi.org/10.1021/acs.jctc.2c01180.
- ⁸⁰ A. B. Robles, P.-A. Hofmann, T. Chuna, T. Dornheim, and M. Hecht, "Pylit: Reformulation and implementation of the analytic continuation problem using kernel representation methods," (2025), arXiv:2505.10211 [physics.comp-ph].